International Journal of Multiphase Flow 184 (2025) 105112

Contents lists available at ScienceDirect

International Journal of Multiphase Flow

journal homepage: www.elsevier.com/locate/ijmulflow

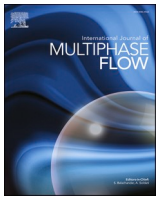

Research Paper

Prediction of bubbly flow and flow regime development in a horizontal air-water pipe flow with a morphology-adaptive multifluid CFD model

Marco Colombo [a,*], Michael Fairweather [b]

[a] School of Mechanical, Aerospace and Civil Engineering, University of Sheffield, Sheffield S1 4DT, United Kingdom
[b] School of Chemical and Process Engineering, University of Leeds, Leeds LS2 9JT, United Kingdom

ARTICLE INFO

Keywords:
Multiphase CFD
Morphology-adaptive multifluid
Gas-liquid flows
Horizontal flows
Flow regimes

ABSTRACT

Most multiphase gas-liquid flows of industrial and engineering interest often encompass multiple flow regimes and the transition between them. The wide range of interface scales involved is challenging to model, and this has so far limited the application of computational fluid dynamics to multi-regime flows and complex multiphase flow conditions. The morphology-adaptive GEneralized Multifluid Modelling Approach (GEMMA), developed in OpenFOAM, is designed to provide all-flow-regime modelling capabilities. The model implements in the multifluid modelling framework interface-resolving capabilities that are used to treat large-scale interfaces found in segregated flow regimes, while dispersed regimes remain modelled with the standard multifluid approach. In this paper, GEMMA is used to predict, for the horizontal pipe flow studied in the METERO experiment (Bottin et al., 2014), the development of the bubbly, plug, slug and stratified flow regimes starting from a homogeneous 1 mm bubble distribution at the inlet of the pipe. In the bubbly regime, the model predicts well the void fraction and bubble diameter distributions, but not the lower flow velocity when a bubble layer accumulates at the top of the pipe. Results also show that modelling closures developed mainly for vertical flow conditions, and which are a strong function of the relative velocity, may not be equipped to predict horizontal flows where relative velocities can be negligible. Beyond the bubbly regime, the model predicts the development of intermittent gas plugs, the increase in the length scale of the plugs approaching the transition to slug flow and the development of a stratified flow at the lowest water flow rate. The velocity of gas plugs is found to be in good agreement with literature models. Challenging to predict remains the transition region from bubbly to plug and from slug to stratified flow, where an anticipated transition to stratified flow is predicted in the slug regime. Overall, GEMMA provides a morphology-adaptive modelling framework that can achieve all-flow regime applicability, and the present work is a first demonstration of its capabilities for horizontal flow regimes. Short-term development needs are highlighted, such as additional validation and the improvement of bubbly flow closures, and the modelling of the dispersion and breaking-up of large interfaces to prevent excessive phase agglomeration.

1. Introduction

Multiphase gas-liquid flows are frequent in engineering, industrial systems, and everyday life, and even so they remain one of the most challenging areas of fluid dynamics. The many possible arrangements between the phases each impact in a different way the interface physics and the thermo-fluid dynamics of the flow. When many tiny bubbles are dispersed in a background continuous liquid, the flow behaves differently compared to a stratified flow where gas and liquid streams are separated by a large continuous interface. These two extremes, and the other many possible arrangements in-between, have been historically classified in flow regimes based on the interface morphology and the phases behaviour (Collier and Thome, 1994).

The first flow maps, where flow regimes are classified based on different dimensional or non-dimensional parameters, were developed in the 50's and 60's and have found significant application since (Baker, 1954; Hewitt and Roberts, 1969). Flow regime maps have been constantly developed and improved over the years (Rouhani and Sohal, 1983; Cheng et al., 2008; Wu et al., 2017), encompassing a wide range of geometries, including mini and micro channels (Chinnov et al., 2016; Shin and Kim, 2022), and fluid mixtures, taking advantage of progress made in measuring techniques and more recently leveraging data-driven

* Corresponding author.
E-mail address: m.colombo@sheffield.ac.uk (M. Colombo).

https://doi.org/10.1016/j.ijmultiphaseflow.2024.105112
Received 21 July 2024; Received in revised form 15 November 2024; Accepted 16 December 2024
Available online 17 December 2024

and machine learning methods (Zhang et al., 2020; Hibal et al., 2022). They remain the primary choice to estimate the flow regime in complex industrial equipment and in one-dimensional fluid dynamic models, such as system codes extensively used in nuclear reactor thermal hydraulics safety analyses (Roth and Aydogan, 2014). However, each map is limited to a specific geometry and conditions, and some uncertainties always exist in the precise location of phase boundaries, particularly for maps based on the visual identification of regimes from experiments.

Computational fluid dynamics (CFD), by solving the entire range of flow and interface scales in a multiphase flow, may in principle provide a computational tool that can predict the development and the main flow features of all flow regimes. However, models that effectively solve all physical scales, developed by coupling direct numerical simulation with interface-resolving techniques (Sussman et al., 1999; Tryggvason et al., 2001), quickly become computationally challenging (Cifani et al., 2018; Fang et al., 2018) in high Reynolds number flows, large domains or in dispersed regimes such as bubbly flows over a certain bubble concentration. Currently, these models excel at extracting flow physics and interface process knowledge and understanding from fully resolved simulations of simplified and controlled flow conditions. This knowledge then informs the development of lower-fidelity CFD modelling closures (Feng and Bolotnov 2017, 2018; Ma et al., 2020; du Cluzeau et al., 2022; Jin et al., 2023). These closures are employed in Eulerian-Eulerian multifluid models, which are the go-to method when addressing multiphase flows at the industrial or equipment scale. In multifluid models, the instantaneous flow field and phase distribution are averaged, the interface scales filtered out and the interface physics entirely modelled using closure laws (Ishii and Hibiki, 2006; Yeoh and Tu, 2010). However, interface physics depends on the flow regime and available closure laws are regime-dependent, which limits the applicability of multifluid models (Bestion, 2014). The majority of studies have focused on bubbly flows, where the dispersion of a large number of small bubbles on a background continuous phase has been successfully predicted by averaging coupled to a population balance model in a wide range of flow conditions (Hosokawa and Tomiyama, 2009; Liao et al., 2015; Colombo and Fairweather, 2016; Colombo et al., 2021; Lahey Jr. et al., 2021). More limited have been the applications to other regimes such as slug, plug or churn flows. Other than requiring different closure laws, in these regimes the phases are segregated in large continuous, intermittent structures separated by large-scale interfaces, features that are challenging to capture with averaged multifluid models. Stratified flows have been successfully predicted with interface-resolving methods, for Reynolds numbers up to 10,000 (Komen et al., 2023), but the full resolution of even a single Taylor bubble in the slug regime requires massive computational resources (Zimmer and Bolotnov 2019; Kren et al., 2024). Overall, multiphase CFD is still limited in its ability to model the wide range of interface scales found in multi-regime flows and flow regime transition, which are conditions that are often encountered in industrial flows and engineering processes (Bestion, 2014).

Overcoming these limitations and coping with the multiscale nature of multi-regime multiphase flows is the aim of morphology-adaptive Eulerian-Eulerian models, where different degrees of interface resolution capabilities are implemented into the multifluid description. First attempts coupled the multifluid with the volume of fluid (VOF) interface-capturing method, with the switching between the two frameworks governed by the local behaviour of the gas volume fraction (Cerne et al., 2001). The need to switch from a multifluid to a single-fluid representation, changing the number of conservation equations in the same computational domain, has proven challenging numerically (Strubelj et al., 2009; Gada et al., 2017). Further and more recent developments have therefore opted for implementing some degree of interface resolution directly inside the multifluid framework (Strubelj et al., 2009; Marschall, 2011; Coste, 2013; Gada et al., 2017; De Santis et al., 2021; Frederix et al., 2021; Schlegel et al., 2023). In these models, a set of conservation equations is still solved for each phase and interface transfers modelled. However, when large-scale, segregated interfaces are identified, "sharpening" algorithms are used to counteract multifluid numerical diffusion and maintain the local shape of the interface, and closures employed are selected based on the local interface morphology.

Coste (2013) developed the Large Interface Model (LIM), where large interfaces are identified from the volume fraction gradient becoming higher than a fixed threshold value. Once the interface has been detected, a three-cell stencil is built, with the centre cell belonging to the interface, and one to each of its sides belonging to the continuous liquid and gas phases. At large interfaces, interface momentum exchange considers the surface tension and the interface drag, modelled with an anisotropic model assuming a wall law behaviour on both sides of the interface. Initially developed for stratified flows, the model has been implemented in the NEPTUNE_CFD software and extended to the Generalized Large Interface Model (GLIM) (Mer et al., 2018) to handle the full range of regimes from bubbly to droplet flows.

The Hybrid Dispersed-Large Interface Solver (HD-LIS) (Mathur et al., 2019) was developed in OpenFOAM by the Nuclear Research and Consultancy Group. The large interfaces are identified from a flow regime map using the local value of the volume fraction, and a compression term in the continuity equation is used to maintain the interface sharp. In regions of large interfaces, interface momentum transfer is modelled by considering drag, modelled following Marschall (2011), and the surface tension force. The HD-LIS treats each phase as a single field. The model was later extended by Frederix et al. (2021) to a four-field model, the Four-Field Large Simulation (FF-LIS) model, which includes a dispersed and a continuous field for each of the two phases and individual conservation equations for each field.

Researchers at Helmholtz-Zentrum Dresden-Rossendorf developed the morphology-adaptive multifield model MultiMorph (Meller et al., 2020; Wang et al., 2023), also implemented in OpenFOAM. MultiMorph solves for separate dispersed and continuous fields for each of an arbitrary number of phases. The large interfaces are detected using the value of the volume fraction, and a compression term is included to keep the interface sharp (Yin et al., 2023). The interface momentum exchange at large interfaces is modelled with the drag model of Strubelj and Tiselj (2011) and includes the surface tension force.

The GEneralized Multifluid Modelling Approach (GEMMA), developed by De Santis et al. (2021), is also implemented in OpenFOAM. Differently from the above models, large interfaces are detected using the local resolution of the interface curvature on the grid and the average diameter of the dispersed phase, or the local gradient of the void fraction. Modelling of the momentum exchange at large interfaces includes the drag and the surface tension force, and a compression term is included to keep large interfaces sharp.

So far, these models have been mostly applied to validation cases to assess their performance in specific regimes or in conditions where a mix of large and dispersed interfaces exist. Most of the time, the regime to predict was known *a priori*. Instead, a systematic study of a model's ability to predict the development of different regimes, starting from generic initial conditions, and to adapt the model formulation to the local development of the flow and the length scale of the interfaces is missing. In this paper, the GEMMA model is used to predict multiphase gas-liquid flow conditions in a horizontal pipe and the development of bubbly, plug, slug and stratified flow regimes starting from a homogeneous bubbly flow at the inlet of the pipe. The model performance is assessed by comparing predictions with experimental measurements from the METERO experiment (Bottin et al., 2014), where the development of these regimes in a horizontal pipe was studied. Using the data available from METERO, the first part of the paper specifically focuses on the model accuracy in the bubbly regime, given that CFD models have been extensively validated in vertical pipes but much less so in horizontal pipes. Exceptions are the work of Yeoh et al. (2012), who used ANSYS CFX to predict the pipe flow experiments of Kocamustafaogullari and Huang (1994), and Ekambara et al. (2012), who also used ANSYS CFX to predict the experiments of Kocamustafaogullari and

Wang (1991) and Kocamustafaogullari and Huang (1994). More recently, Mimouni et al. (2017) have used the METERO experiment to validate a large bubble model implemented to resolve continuous gas structures in the multifluid model of NEPTUNE_CFD. Differently from GEMMA, in the model of Mimouni et al. (2017) large interfaces are identified from the cell value of the volume fraction. Different authors have instead applied the VOF model to predict the plug and slug regimes (Deendarlianto et al., 2016; Nasrfard et al., 2019). However, the model does not provide accurate results in the bubbly regime (Pinilla et al., 2019), unless the grid is refined to a resolution unmanageable in most bubbly flows of practical interest. Instead, in this paper the GEMMA model is used to predict the development of all the horizontal gas-liquid pipe flow regimes studied in the METERO experiment.

2. CFD model

The GEMMA model is implemented conjointly with the native OpenFOAM Foundation OpenFOAM 9 *multiphaseEulerFoam* multifluid solver (The OpenFOAM Foundation, 2021). *multiphaseEulerFoam* solves for a set of mass, momentum and energy conservation equations for each of n compressible phases and can account for mass and energy transfers at the interface and phase change. GEMMA implements inside this multifluid solver a methodology to detect large interfaces and model continuous intermittent phase structures and segregated flow regimes the standard multifluid model struggles to cope with. Large interfaces are identified from the resolution of the interface curvature and the average length scale of the dispersed field or the local void fraction gradient, and maintained sharp by activating a compression term in the mass conservation equation. Closure laws, always needed to model interface transfers, are selected based on the local flow regime, applying proper modelling closures for large, sharp interfaces.

Given that adiabatic flows are considered in this work, the model solves for a set of mass and momentum conservation equations for each phase:

$$\frac{\partial}{\partial t}(\alpha_k\rho_k) + \nabla\cdot(\alpha_k\rho_k\boldsymbol{U}_k) + \nabla\cdot[\alpha_k(1-\alpha_k)\rho_k\boldsymbol{U}_c] = 0 \tag{1}$$

$$\frac{\partial}{\partial t}(\alpha_k\rho_k\boldsymbol{U}_k) + \nabla\cdot(\alpha_k\rho_k\boldsymbol{U}_k\boldsymbol{U}_k) = -\alpha_k\nabla p + \nabla\cdot\left[\alpha_k\left(\boldsymbol{\tau}+\boldsymbol{\tau}^{Re}\right)\right] + \alpha_k\rho_k\boldsymbol{g} + \boldsymbol{M}_k \tag{2}$$

In the previous equations, α, ρ and $\boldsymbol{U}$ are the volume fraction, density and velocity of each phase, which is identified by the subscript k. p is the pressure, $\boldsymbol{g}$ the gravitational acceleration, and $\boldsymbol{\tau}$ and $\boldsymbol{\tau}^{Re}$ the viscous and turbulent stress tensors. $\boldsymbol{M}_k$ is the interface momentum transfer that models the dynamic interaction between the phases. The third term in Eq. (1) is the compression term that maintains large interfaces sharp by counteracting numerical diffusion that affects multifluid fields in the presence of sharp gradients. Such compression, usually included in a similar form in hybrid, morphology-adaptive multifluid models (Wardle and Weller, 2013; Mathur et al., 2019; Frederix et al., 2021), is purely numerical, and it is also often used to avoid numerical diffusion of the interface in VOF models (Berberovic et al., 2009). $\boldsymbol{U}_c$ is the compression velocity which acts in a direction normal to the interface, identified from the volume fraction gradient, and it is proportional to the relative velocity between the phases $\boldsymbol{U}_r$:

$$\boldsymbol{U}_c = C_\alpha|\boldsymbol{U}_r|\frac{\nabla\alpha}{|\nabla\alpha|} \tag{3}$$

In Eq. (3), C_α is the scalar field that identifies the regions of the domain where a large interface is present and ensures the action of compression is limited to these regions. It is equal to 1 in cells occupied by large interfaces, and 0 in dispersed regions or when continuous regions of the same phase already exist. The value of the C_α field is established by the large interface detection algorithm.

2.1. Large interface detection

The C_α field governs the interface compression and the blending of the interface closures depending on the local topology of the interface. Large interfaces are identified from the multifluid field by estimating their length scale and the resolution of the interface curvature allowed by the computational grid. In the context of numerical modelling, large interface is a relative term and has significance only if related to the computational grid used to resolve it (i.e., when finely resolved, a small bubble can be considered a large interface (De Santis et al., 2021)). By selecting the minimum length scale and desired mesh resolution, we are also able to control and select the interface scales that need to be resolved. The mesh resolution is monitored by the interface resolution quality (*IRQ*) and needs to be higher than a minimum threshold for an interface to be classified as large:

$$IRQ = \frac{2}{\Delta\kappa} > IRQ_{crit} \tag{4}$$

In Eq. (4), Δ is the local mesh size and κ is the interface curvature, which is estimated from $\kappa = -\nabla\cdot(\nabla\alpha/|\nabla\alpha|)$. Higher values of *IRQ* corresponds to a more resolved interface. In this work, the critical value is assumed equal to 2, as previously validated in applications of the GEMMA model in several flow conditions (De Santis et al., 2021). In this work, in cells where the *IRQ* condition is met, the large interface formulation is activated if the local dispersed phase size, identified from the Sauter-mean diameter of that phase, is higher than a value expressed as Γ-times the mesh size Δ:

$$d_{SM} > \Gamma\Delta \tag{5}$$

Alternatively, although not used in this work, the length scale can be estimated from the local volume fraction gradient (Colombo et al., 2022). At the present time, the two criteria are mutually exclusive. Finally, the large interface formulation is deactivated in continuous regions where the void fraction is higher than 0.99 or lower than 0.01.

2.2. Blended closure modelling framework

In Eq. (2), $\boldsymbol{M}_k$ is the interface momentum transfer and models momentum exchanges between the phases as a sum of forces, in particular the drag ($\boldsymbol{F}_d$), lift ($\boldsymbol{F}_l$), wall lubrication ($\boldsymbol{F}_w$), virtual mass ($\boldsymbol{F}_{vm}$), turbulent dispersion ($\boldsymbol{F}_{td}$) and surface tension ($\boldsymbol{F}_{st}$) forces:

$$\boldsymbol{M}_k = \boldsymbol{F}_d + \boldsymbol{F}_l + \boldsymbol{F}_w + \boldsymbol{F}_{td} + \boldsymbol{F}_{vm} + \boldsymbol{F}_{st} \tag{6}$$

All forces except surface tension are included in dispersed regions. A large interface drag model and surface tension model are used to determine the momentum transfer across large interfaces. Blending between regimes is obtained by joining the native OpenFOAM blending function with the C_α field. The OpenFOAM hyperbolic function is used to blend the gas dispersed in liquid (e.g. bubbly flows) to liquid dispersed in gas (e.g. droplet flows), with transition occurring at 0.5 void fraction. The C_α field overwrites this function, enforcing large interface modelling in cells occupied by large-scale interfaces. For the drag force, the blended model reads:

$$\boldsymbol{F}_d = \left[1-(1-C_\alpha)f_{gl}-(1-C_\alpha)f_{lg}\right]\boldsymbol{F}_{d,LI} + (1-C_\alpha)f_{gl}\boldsymbol{F}_{d,gl} + (1-C_\alpha)f_{lg}\boldsymbol{F}_{d,lg} \tag{7}$$

In Eq. (7), *LI* identifies the large interface drag model and *gl* and *lg* the dispersed gas in liquid and liquid in gas drag closures and blending functions f. In dispersed regions, the drag is modelled according to Ishii and Zuber (1979) for gas dispersed in liquid and Schiller and Naumann (1935) for liquid dispersed in gas. The drag force at large interfaces is instead modelled using the segregated interface model from Marschall (2011):

$$\boldsymbol{F}_{d,LI} = \left[0.5 \frac{\rho_m \delta |\boldsymbol{U}_g - \boldsymbol{U}_l|}{\frac{\alpha_g \alpha_l \mu_g \mu_l}{\mu_g + \mu_l}} + 8 \frac{\frac{\alpha_g \alpha_l \mu_g \mu_l}{\alpha_g \mu_l + \alpha_l \mu_g}}{\frac{\mu_g \mu_l}{\mu_g + \mu_l}} \right] \frac{|\nabla \alpha|}{\delta} \frac{\mu_g \mu_l}{\mu_g + \mu_l} (\boldsymbol{U}_g - \boldsymbol{U}_l). \tag{8}$$

In Eq. (8), μ is the dynamic viscosity, ρ_m the volume fraction weighted mixture density and δ the width of the interface, modelled as $1/|\nabla \alpha|$ (Marschall, 2011). Lift, wall lubrication, virtual mass and turbulent dispersion are accounted for in dispersed regions:

$$\boldsymbol{F}_{(l,w,vm,td)} = (1 - C_\alpha) f_{gl} \boldsymbol{F}_{gl} + (1 - C_\alpha) f_{lg} \boldsymbol{F}_{lg} \tag{9}$$

A constant lift force coefficient is used, $C_l = 0.1$ (Colombo and Fairweather, 2015, 2019, 2020), and the virtual mass coefficient is also constant, $C_{vm} = 0.5$. The wall force is modelled according to Hosokawa et al. (2002) and the turbulent dispersion, following a sensitivity study summarized in Section 5.1, is taken from Lopez de Bertodano (1998).

At large interfaces, the surface tension force is also considered:

$$\boldsymbol{F}_{st} = C_\alpha \boldsymbol{F}_{st,LI} \tag{10}$$

This force is modelled as a force per unit volume from the continuum surface force method of Brackbill et al. (1992):

$$\boldsymbol{F}_{st,k} = \alpha_k \sum_{i=1}^{n_k} C_{\alpha,ki} \sigma_{ki} \kappa \nabla \alpha \frac{2 \rho_m}{\Delta \rho_{ki}} \tag{11}$$

where σ is the surface tension. The curvature is estimated from the volume fraction field, smoothed by successive interpolation from cell centres to faces to limit the appearance of parasitic currents (Ubbink, 1997). Given that the density ratio is normally large in gas-liquid mixtures, a density correction is also included (Heyns and Oxtoby, 2014; De Santis et al., 2021). More than two phases can be present in the same cell, so the surface tension force is calculated for each phase k by summation over all the n_k phases that share an interface with k in the cell and weighted using the cell phase volume fraction.

2.3. Turbulence modelling and population balance model

Turbulence is modelled using a mixture $k - \varepsilon$ RANS turbulence model, which solves balance equations for the mixture turbulence kinetic energy k_m and the mixture turbulence kinetic energy dissipation rate ε_m (Behzadi et al., 2004):

$$\frac{\partial}{\partial t}(\rho_m k_m) + \nabla \cdot (\rho_m k_m \boldsymbol{U}_m) = \nabla \cdot (\mu_m^{tot} \nabla k_m) + P_m - \rho_m \varepsilon_m + S_{k,m} \tag{12}$$

$$\frac{\partial}{\partial t}(\rho_m \varepsilon_m) + \nabla \cdot (\rho_m \varepsilon_m \boldsymbol{U}_m) = \nabla \cdot (\mu_m^{tot} \nabla \varepsilon_m) + C_1 P_m \frac{\varepsilon_m}{k_m} - C_2 \rho_m \frac{\varepsilon_m}{k_m} \varepsilon_m + S_{\varepsilon,m} \tag{13}$$

In Eqs. (12) and (13), $\boldsymbol{U}_m$ is the mixture velocity, ρ_m is the mixture density, obtained from the weighted averaging of the phase densities, and P_m is the turbulence production due to shear, obtained from the mass-weighted averaging of the phase-specific turbulence productions. In segregated regimes, where large regions of continuous gas and liquid are found, the use of a mixture model improves stability. It avoids solving for phase-related turbulence quantities of the other phase in continuous regions, where large oscillations in the production and dissipation of turbulence are often found solving phase-specific turbulence models.

Mechanisms of turbulence production and dissipation at the interface are accounted for with source terms $S_{k,m}$ and $S_{\varepsilon,m}$. In dispersed bubbly flow regimes, bubble-induced turbulence is accounted for and modelled using the model proposed by Rzehak and Krepper (2013) that assumes the drag force is converted into turbulence kinetic energy in the bubble wake. A mechanism of turbulence suppression near large interfaces is also included by a source of turbulence dissipation at the interface. This additional dissipation is necessary to predict the wall-like behaviour on the gas-side of the interface and avoid the generation of unphysical levels of turbulence in the interface region and it is modelled following Frederix et al. (2018). Dispersed and large interface mechanisms are blended with the same method used for interface momentum transfer, so that interface suppression is active only for large interfaces, and bubble-induced turbulence in gas dispersed in liquid regimes. In the below equations, the parameters $C_{k,BI}$ and $C_{\varepsilon,BI}$ are equal to 1.0, and the parameter δ is 10^{-4} (Frederix et al., 2018):

$$S_{k,m} = (1 - C_\alpha) f_{gl} C_{k,BI} \boldsymbol{F}_{d,gl} \boldsymbol{U}_r \tag{14}$$

$$S_{\varepsilon,m} = (1 - C_\alpha) f_{gl} C_{\varepsilon,BI} \frac{k^{0.5}}{d_B} \boldsymbol{F}_{d,gl} \boldsymbol{U}_r + C_\alpha \sum_{k=l,g} \left[C_2 \alpha_k \rho_k \left(\frac{\nu_k}{\delta^2} \right)^2 k_k \right] \tag{15}$$

In dispersed regimes, the interface transfer processes are driven by the size distribution of the dispersed phase and the interfacial area in the flow. This size distribution is governed by bubble coalescence and breakup caused by the interaction of bubbles with the fluid and neighbour bubbles. In GEMMA, the average bubble diameter is also used to establish the presence of large interfaces and trigger the large interface operation of the model (Eq. (5)). To predict the bubble size distribution and the bubble average diameter, GEMMA is coupled with the OpenFOAM *multiphaseEulerFoam* class-based population balance model. The model approximates the bubble diameter distribution as discrete, by dividing the diameter space into a finite number of classes and solving a transport equation for each class (Kumar and Ramkrishna, 1996; Liao et al., 2018):

$$\frac{\partial}{\partial t}\left(\alpha_k \rho_k f_{k,i}\right) + \nabla \cdot \left(\alpha_k \rho_k \boldsymbol{U}_k f_{k,i}\right) = B_{b,i} - D_{b,i} + B_{c,i} - D_{c,i} \tag{16}$$

In Eq. (16), $f_{k,i}$ is the volume density of bubbles of phase k with diameter i normalized by the total volume fraction of phase k, equal to the fraction of the total gas volume occupied by bubbles of class i. On the right-hand side of Eq. (16), B is the class i volume fraction birth rate due to breakup (subscript b) from an upper class and coalescence (subscript c) of smaller bubbles. D instead identifies the corresponding death rates. Coalescence is modelled following Lehr et al. (2002) and breakup with the model of Luo and Svendsen (1996). Sensitivity to the coalescence model, which has by far the largest impact on the bubble distribution in the simulated pipe flows, is included in the results section. The Sauter-mean diameter, used by the interface transfer closures and in the large interface detection algorithm, is calculated as:

$$d_{SM,k} = \frac{1}{\sum_{i=1}^{I} \frac{f_{k,i}}{d_{k,i}}} \tag{17}$$

where $d_{k,i}$ is the diameter of class i of phase k and I the total number of classes.

3. METERO experiment

In this work, GEMMA is used to model the METERO experiment (Bottin et al., 2014). The METERO experiment studied the flow regime transition in a horizontal pipe of diameter 0.1 m and length 5.4 m. 1 mm diameter air bubbles were injected in the continuous liquid flow and, starting from the bubbly flow, the transition to plug, slug and stratified regimes triggered by progressively reducing the liquid flow rate at a fixed gas flow rate, increasing the gas volume fraction. Superficial velocity was in the range 0 – 5.3 ms^{-1} for the water and 0 – 0.7 ms^{-1} for the air. The flow regime was identified from top and lateral views of the flow provided by a high-speed video camera. Velocity and turbulence in the liquid phase were measured using a hot-film anemometer, and bubble diameter and velocity with two optical probes. Measurements are available across the radius at distances of L/D equal to 5, 20 and 40 from the inlet, although only for the bubbly flow regime, and these will be used to assess the predictions of the model described.

The 7 conditions summarized in Table 1 were selected, two in the

Table 1
Experimental tests predicted with GEMMA.

Case	j_w $[ms^{-1}]$	j_a $[ms^{-1}]$	α $[-]$
BB	4.42	0.063	0.014
SB	3.55	0.063	0.021
SB2P	2.4	0.063	0.0256
P	2.0	0.063	0.0305
P2SL	1.5	0.063	0.0403
SL	1.0	0.063	0.059
ST	0.4	0.2	0.333

bubbly regime, one for the buoyant (BB) and one for the stratified bubbly (SB) regimes, one each in the plug (P), slug (SL) and stratified (ST) regimes, one in the transition region from bubbly to plug (SB2P) flow and one from plug to slug (P2SL) flow. In the experiment, the bubbly regime is distinguished between buoyant and stratified bubbly. In the buoyant bubbly regime, bubbles flow in a dispersed pattern in the upper region of the pipe, where they migrate due to buoyancy. In the stratified bubbly regime, a bubble layer is formed near the top of the pipe. Bubbles in the layer behave differently than bubbles outside the layer, namely having a lower velocity, but coalescence is not yet sufficient to form large air plugs (Bottin et al., 2014). All the simulations were made with an air superficial velocity of 0.063 ms^{-1} (except for the stratified regime, where $j_a = 0.2$ ms^{-1}), and the water velocity was progressively reduced from 4.42 ms^{-1} in the bubbly regime to 0.4 ms^{-1} in the stratified regime.

4. Computational mesh and numerical settings

The 5.4 m long pipe used in the METERO experiment was modelled in a three-dimensional computational domain. The length of the pipe is sufficient to have flow unperturbed from the outlet boundary condition at $L/D = 40$, where results are compared against experiments. It is also sufficient for the flow to complete the flow regime transition starting from the uniform velocity and void fraction profiles imposed at the inlet, matching the experimental superficial velocities. Pressure is imposed at the outlet, and a no-slip condition on both phases and a high-Re turbulence wall treatment are imposed at the pipe wall.

The population balance model includes 8 bubble classes covering the range 0.5 – 8 mm. At the inlet, a unform distribution of 1 mm diameter bubbles is imposed, matching inlet experimental conditions. After the inlet, the impact of break-up is minimal, and the bubble diameter rarely falls below 1 mm. The upper limit of the bubble range is instead imposed considering the criteria for the transition to a large interface that is imposed at 6 mm (Eq. (5)). In vertical pipes, this is the diameter at which the lift force changes sign and starts pushing large bubbles towards the pipe centre, to a certain extent initiating the transition from a bubbly to a slug flow regime. In view of this, the selection of the maximum bubble diameter value is consistent. Larger bubbles are resolved by the large interface formulation and do not need to be tracked by the population balance model. In addition, the presence of the upper limit ensures that a consistent value of the bubble diameter is used by the population balance when these large interfaces break-up in dispersed bubbly flow regions. For the interface resolution parameter (IRQ_{crit} in Eq. (4)), a value of 2 is used in line with previous works (De Santis et al., 2021; Colombo et al., 2022).

The convective terms are discretized using second-order schemes, and the transient term with a first-order implicit scheme. The volume fraction equations are solved with the semi-implicit multidimensional limiter for explicit solution (MULES) approach (Berberovic et al., 2009; Mathur et al., 2019), and the pressure-velocity coupling is solved using a multiphase extension of the PIMPLE algorithm (The OpenFOAM Foundation, 2021). Simulations were run for a maximum of 20 seconds, long enough to characterize parameters in unsteady regimes, such as the average velocity of the Taylor bubbles in the plug and slug regimes. Shorter run times were sufficient for dispersed regimes. The time-step was fixed to remain below 0.4 of the flow Courant number. Given the diverse conditions tested, this covers a large range of values, but usually in the range $1{\cdot}10^{-3}$ – $1{\cdot}10^{-4}$s.

Prior to the simulations, a grid sensitivity study was made with meshes having 286,720, 560,000 and 1,193,400 elements. Results are reported in Fig. 1 for the air velocity, the void fraction, the streamwise normal turbulent stress and the turbulence dissipation rate for the water phase in the bubbly flow regime. In these and in all following plots unless stated otherwise, results are taken at distance from the inlet $L/D = 40$, along the radius of the pipe aligned with the vertical direction. Values on the x-axis are normalized by the pipe diameter and the zero value corresponds to the pipe centre. Results from the three meshes are very similar, with the less-refined mesh (Mesh 1) showing slightly larger changes in the near-wall regions. Consequently, Mesh 2 was used in all simulations included hereafter.

5. Results and discussion

5.1. Model sensitivity

As highlighted in the modelling section, CFD predictions depend on interface momentum transfer and the average diameter of the bubbles predicted by the population balance approach, and the accuracy of the modelling closures employed has a critical impact on the performance of the model. Specifically, turbulent dispersion and bubble coalescence were found to significantly impact the results and the sensitivity on the modelling of these terms is investigated further in this section.

The model of Burns et al. (2004) is often successfully used to model turbulent dispersion in bubbly flows. However, the large majority of results have been obtained in vertical pipes (Hosokawa and Tomiyama, 2009; Colombo and Fairweather, 2015; Liao et al., 2015; Colombo et al., 2021; Rzehak et al., 2021), where bubbles rise at a higher velocity with respect to the liquid phase due to buoyancy. The model is derived from Favre-averaging of the drag force and, although it includes the turbulent viscosity, it depends strongly on the value of the relative velocity. This relative velocity is not necessarily present in horizontal pipes, where buoyancy is perpendicular to the fluid motion and the bubbles are transported along with the fluid in the horizontal direction. A much smaller relative velocity is established, as shown in Section 5.2, and the bubble velocity can even be slightly lower than the liquid as in the METERO experiment (Bottin et al., 2014). The dispersion predicted with the Burns et al. (2004) model becomes insufficient, as shown in Fig. 2a, where bubble accumulation at the top of the pipe is excessive even when the dispersion coefficient σ_{TD} is decreased by an order of magnitude to 0.1.

Conversely, the use of approaches such as the one proposed by Lopez de Bertodano (1998), where the dispersion is directly proportional to the turbulence in the flow through the turbulence kinetic energy and does not depend on the relative velocity, allows better agreement with experiments to be obtained. The standard model, with a value of the coefficient C_{TD} of 1, provides the best accuracy in the bubbly regime. However, it predicts excessive accumulation at higher void fractions in the stratified bubbly regime. Therefore, given our aim to predict the entire range of regimes, we opted for a higher value of 1.50 that, despite a little loss of accuracy in the bubbly regime, provided the best overall accuracy. It is important to point out here that this value works for the flows in this paper but by no means should be considered universal. In the past, values from 0.1 up to 500 were used depending on the flow under study (Lavieville et al., 2017), and the development of an improved turbulent dispersion formulation remains a requirement for the accurate prediction of the void distribution in bubbly flows.

In the METERO experiment, bubble diameter evolution was mainly affected by bubble coalescence, with a negligible contribution from break-up. Therefore, prediction of the average bubble diameter mainly depends on the bubble coalescence model used. In Fig. 2b, results from

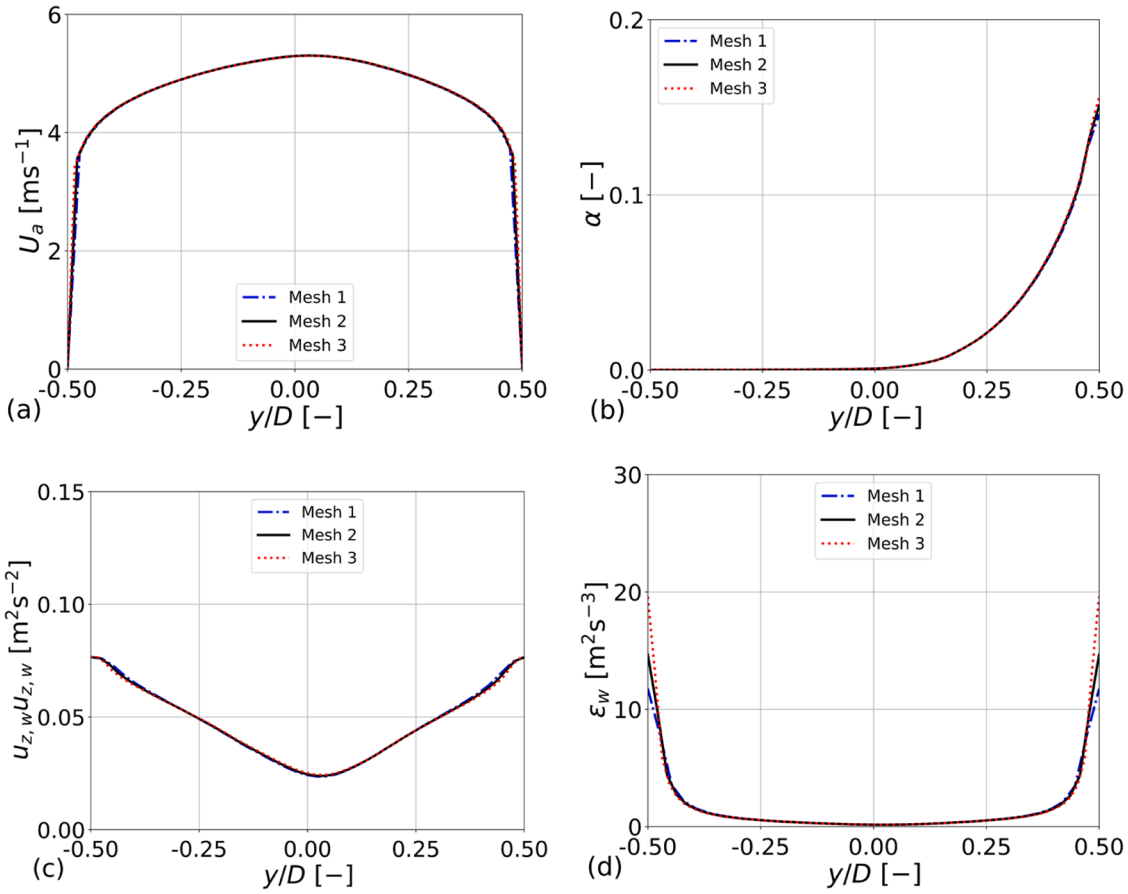

Fig. 1. Mesh sensitivity for the horizontal pipe in the BB regime. Mesh 1 has 286,720 cells, Mesh 2 has 560,000 cells and Mesh 3 has 1,193,400 cells. Profiles are taken on the vertical axis of the horizontal pipe cross section at $L/D = 40$. (a) Air velocity; (b) air volume fraction; (c) water streamwise turbulent normal stress; (d) water turbulence dissipation rate.

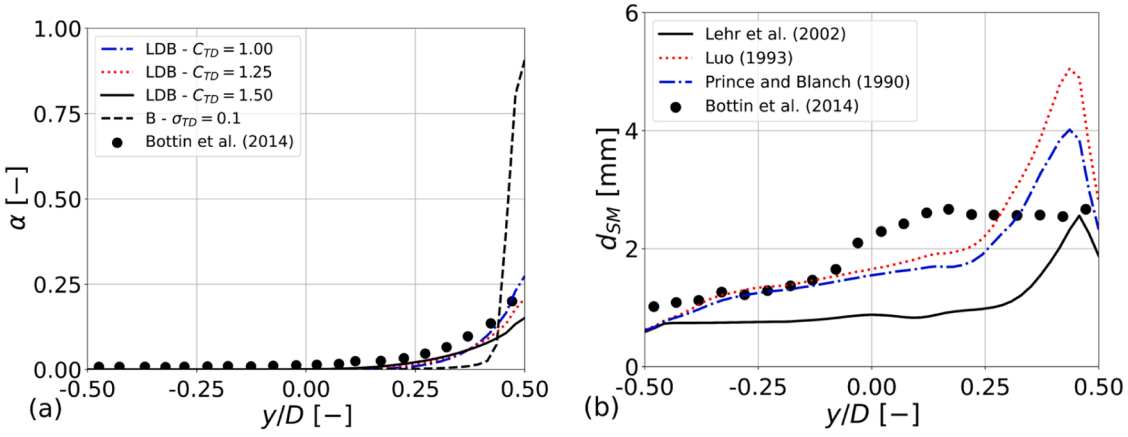

Fig. 2. Sensitivity to the models used for turbulent dispersion and bubble coalescence in the bubbly flow regime. (a) Vertical profile of volume fraction at $L/D = 40$; (b) vertical profile at $L/D = 40$ of the Sauter-mean diameter (LDB – Lopez de Bertodano (1998); B – Burns et al. (2004)).

the model of Lehr et al. (2002), Luo (1993) and Prince and Blanch (1990) are shown for the bubbly regime. In most of the pipe, the Luo (1993) and Prince and Blanch (1990) models show better agreement, while the Lehr et al. (2002) model predicts negligible coalescence and a diameter equal to the inlet value. In the upper portion of the pipe, however, the Lehr et al. (2002) model is in much better agreement, while the other two models significantly overpredict the diameter. This region, as shown by the void fraction plot in Fig. 2a, is where most of the bubbles are found and this significantly impacts the behaviour of the flow. Outside this area, the number of bubbles is minimal and predictions have a negligible impact on the predicted average diameter and on the evolution of the flow and the flow regime transition. For this reason, we decided to use the Lehr et al. (2002) model. In contrast, with the Luo (1993) and Prince and Blanch (1990) models, the overprediction in regions of meaningful void fraction quickly leads to very large, unrealistic bubble diameters as soon as the void fraction is further increased and even before the transition to the stratified bubbly regime.

5.2. Bubbly and stratified bubbly flow regimes

Simulation results for the bubbly flow regime are summarized in Fig. 3, where water and bubble velocity profiles, the normal streamwise turbulent stress, the turbulence dissipation rate, the volume fraction and the Sauter-mean diameter are compared against experimental measurements.

Experiments show a negative relative velocity and a bubble velocity considerably smaller than the water velocity, at least in regions away from the walls. Conversely, CFD simulations with GEMMA show a negligible relative velocity (Fig. 3a). However, the experimental researchers attributed the difference with the liquid velocity to errors in measuring the air velocity with the optical probe method, due to deformation of the bubbles at first touch with the optical probe (Bottin et al., 2014). Measurements taken on the axis of the pipe with particle image velocimetry coupled with shadowgraphy confirmed this hypothesis and obtained a negligible slip between the phases which is much closer to the CFD predictions. Also, the experimental velocity profile is not symmetric, due to the bubble layer in the upper portion of the pipe slowing down the main flow (Bottin et al., 2014), as previously observed also by other authors (Kocamustafaogullari and Wang, 1991). This effect cannot be captured by the CFD code that instead predicted a symmetric profile (Fig. 3a).

The normal streamwise turbulent stress and the turbulence dissipation rate are compared in Fig. 3b and c. The accuracy is good in the centre of the pipe and decreases approaching the walls, where the

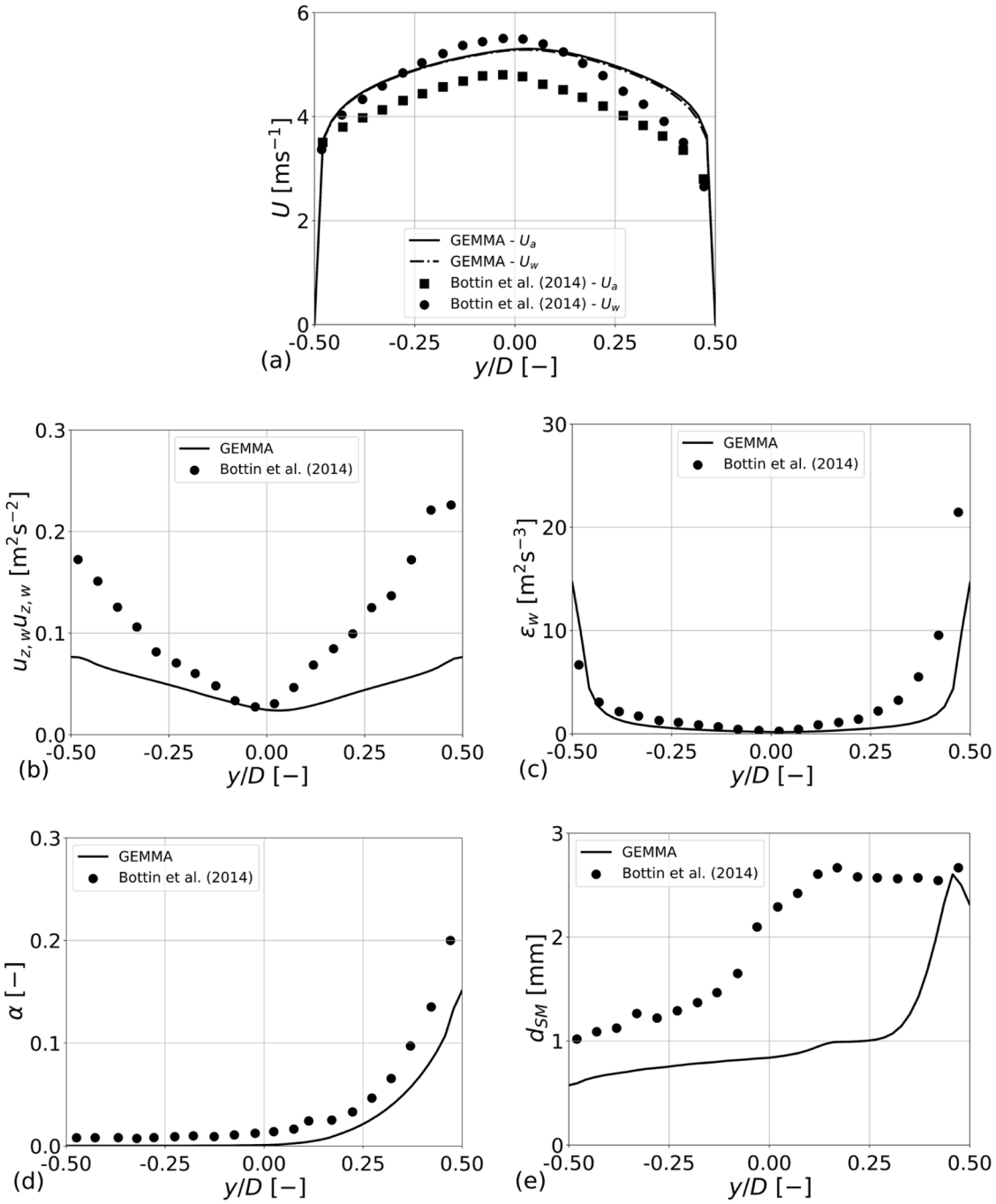

Fig. 3. Predictions compared against the METERO data at $L/D = 40$ for the bubbly flow regime (BB). Plots show profiles of: (a) water and air velocity; (b) streamwise normal turbulent stress; (c) turbulence dissipation rate; (d) void fraction; (e) Sauter-mean diameter.

turbulent stress is significantly underestimated due to the use of wall functions. Closer agreement is shown for the dissipation rate, although as it does for the turbulent stress, the CFD code does not capture the increased turbulence and turbulence dissipation rate at the top, with respect to the bottom, of the pipe induced by the bubbles. Bubble-induced turbulence modelling depends strongly on the relative velocity (Eqs. (14) and (15)) and, as for the turbulent dispersion, works well in vertical pipes but is much less accurate when the relative velocity is negligible such as in horizontal pipes. As noted in Section 5.1, there is a requirement to further develop modelling closures for horizontal pipes, with turbulence and turbulent dispersion modelling having a major impact on the results. As was also already shown in Section 5.1 (Fig. 2), for void fraction and average bubble diameter, in the region where bubbles are effectively present near the top wall void predictions are in good agreement with experiments (Fig. 3d and e). In previous works, such as those of Yeoh et al. (2012) and Ekambara et al. (2012), the correct void fraction distribution was only predicted by artificially limiting the void accumulation at the top of the pipe using a negative value of the lift coefficient, which is however difficult to justify.

Figs. 4a and c, and Fig. 5a, show the instantaneous void fraction, looking down from the top of the pipe and on a pipe cross-section, and the Sauter-mean bubble diameter distributions, from the top of the pipe, for the bubbly regime (BB). Given the length to diameter ratio of the pipe, in these figures the axial pipe length is scaled by a factor 0.2 (the pipe length in the figures appears five times shorter than it is in the computational domain). The figures clearly show how the void fraction accumulates near the upper wall and the model, in this regime, returns the dispersed phase distribution field obtained with multifluid models. In the same figures, the same quantities are shown for the stratified bubbly regime (SB), Figs. 4b and d, and Fig. 5b. For the SB regime, the void fraction near the top wall increases significantly, as does the average bubble diameter driven by enhanced bubble coalescence. The model predicts these increases, but still applies, correctly, the standard multifluid formulation in these dispersed regimes.

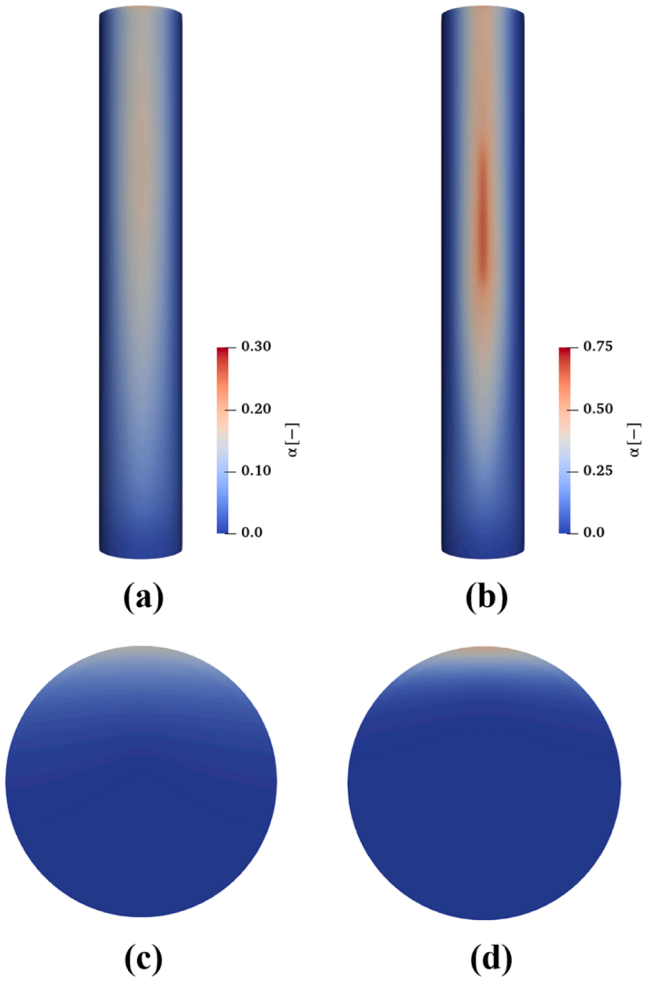

Fig. 4. Top (a and b) and front (c and d) views of the void fraction distribution in the: (a and c) bubbly regime (BB); (b and d) stratified bubbly regime (SB). Axial pipe length is scaled by a factor 0.2 and front views are taken at $L/D = 40$.

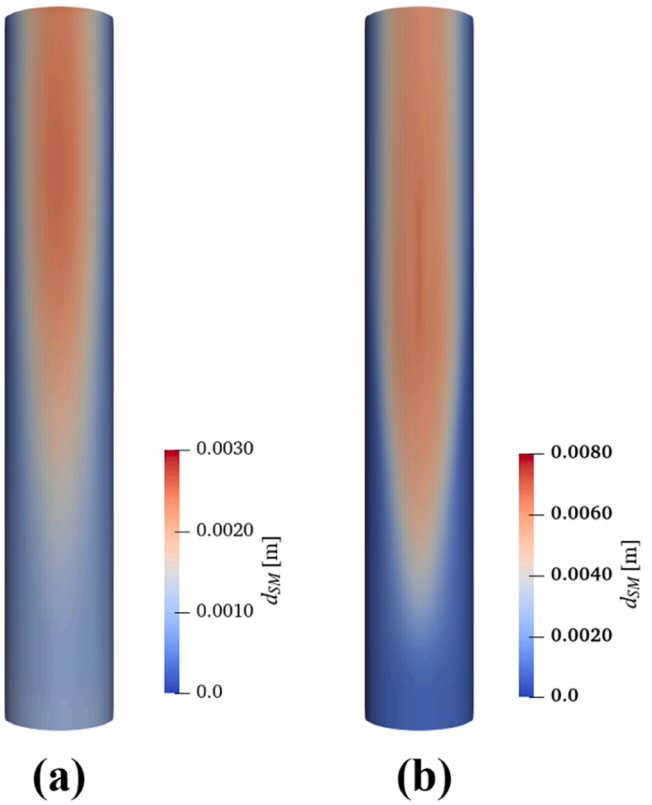

Fig. 5. Top view of the Sauter mean diameter distribution in the: (a) bubbly regime (BB); (b) stratified bubbly regime (SB). Axial pipe length is scaled by a factor 0.2.

Vertical profiles of the void fraction and the Sauter-mean diameter compared between BB and SB are shown in Fig. 6, where the increase in volume fraction and average diameter near the upper wall for SB is evident. It is important to highlight how the prediction of coalescence, already discussed in the sensitivity study of Section 5.1, is critical in keeping model predictions in the dispersed regime range for the BB and the SB cases.

5.3. Segregated regimes

The instantaneous void fraction distribution for regimes other than that of bubbly flow can be found in Fig. 7, where views from the top of the pipe are shown from SB2P on the left to the ST regime on the right. For the latter, the gas occupies the entire upper section of the pipe, and a front view is also included to highlight the stratification. For the same regimes, the instantaneous Sauter-mean diameter distribution is shown in Fig. 8, and the C_α function in Fig. 9. In Fig. 9, the top view is shown for the SB2P, P and P2SL regimes, while a view from the front, to better highlight the stratification, is instead shown for the SL and ST regimes. As done for Figs. 4 and Fig. 5, the axial direction is scaled down and the pipe length reduced 4 times (scaling factor 0.25).

From the stratified bubbly flow regime, a further increase in gas content increases the gas concentration and the coalescence in the upper

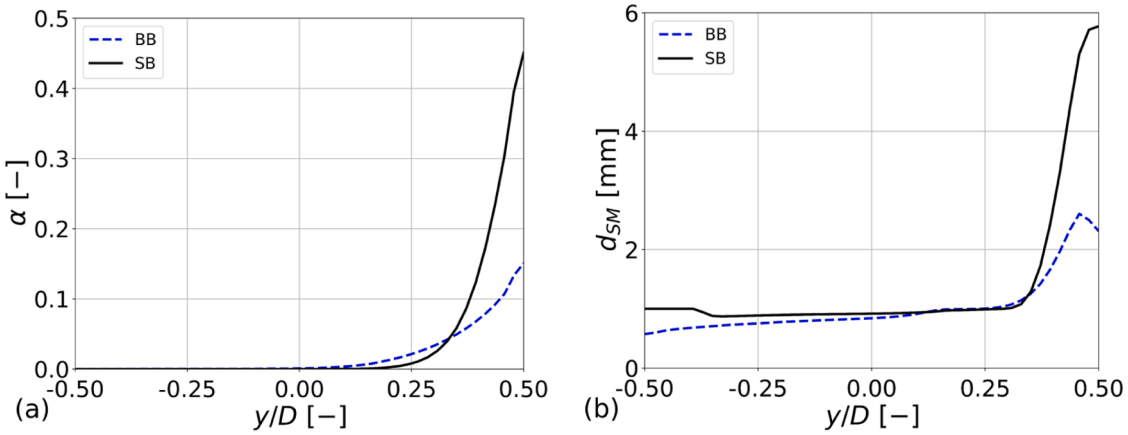

Fig. 6. Vertical profiles at $L/D = 40$ of the void fraction (a) and the Sauter-mean diameter (b) in the BB and SB regimes.

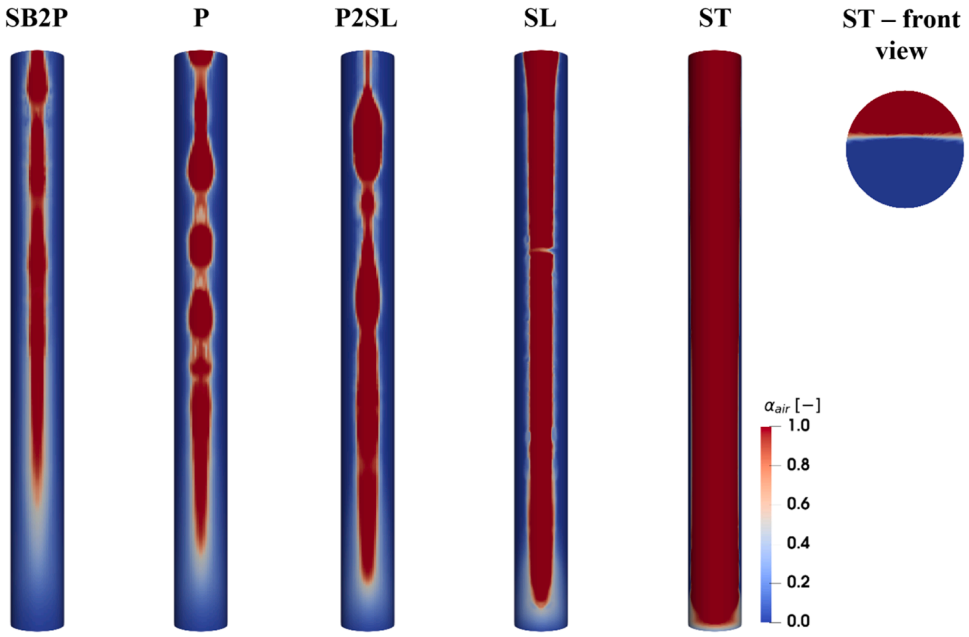

Fig. 7. View from the top of the pipe of the void fraction distribution in the (from left to right) stratified bubbly to plug, plug, plug to slug, slug and stratified flow regimes. On the right, a view of the void fraction distribution on the pip cross-section ($L/D = 40$) in the stratified regime. Axial pipe length is scaled by a factor 0.25.

portion of the pipe, which drives the change in interface morphology with the formation of intermittent continuous gas structures and the transition to the plug and slug regimes. Once the bubble diameter is greater than 6 mm, the model detects and adapts to the presence of large interfaces. In the transition from stratified to plug flow, this occurs only after a certain distance from the inlet (Fig. 8 – SB2P), and in the first half of the pipe large interfaces are only partially recognized, as highlighted by the distribution of C_α in Fig. 9 – SB2P. Consequently, the model only starts to predict the formation of plugs near the end of the pipe, and an almost continuous gas film is instead predicted upstream (Fig. 7 – SB2P), given that the length of the pipe becomes insufficient to complete the transition.

In the plug flow regime, continuous gas plugs that travel along the pipe mixed with dispersed gas regions (Fig. 7 – P) are predicted. The plugs form once the bubble diameter is greater than the large interface threshold, a short distance after the inlet of the pipe (Fig. 8 – P). After this happens, areas of 8 mm diameter bubble regions are found where the plugs are located, alternated with lower diameter bubbles in dispersed or mostly dispersed regions. The upper limit to the bubble diameter range therefore prevents the bubble diameter increasing further in continuous gas regions inside the plugs, where bubbles are not actually present, and the value of the diameter does not impact modelling closures. At the same time, it enables the modelling of lower diameter dispersed bubble pockets in regions between plugs or where large interfaces break-up. In Fig. 9 – P, gas plugs are encircled by thin regions of $C_\alpha = 1$ highlighting the presence of large interfaces.

If the volume fraction is further increased (by reducing the liquid flow rate), longer gas plugs are formed as the flow approaches the slug regime. This increase in the size of the continuous gas region is visible in the predictions for the P2SL case in Figs. 7, Fig. 8 and Fig. 9. These large continuous gas regions remain surrounded by large interfaces identified by $C_\alpha = 1$ in Fig. 9.

In the slug regime (SL), the model predicts an anticipated transition to stratified flow, and it is not able to predict the presence of dispersed regions between gas Taylor bubbles, except from minimum partial separation as shown in Fig. 7 – SL. The bubble diameter quickly reaches 8 mm shortly after the inlet, and never reduces below that value downstream (Fig. 8 – SL). The large interface delineates the continuous gas region in the upper portion of the pipe (Fig. 9 – SL). Similar results are found for the stratified regime, with a larger section of the pipe

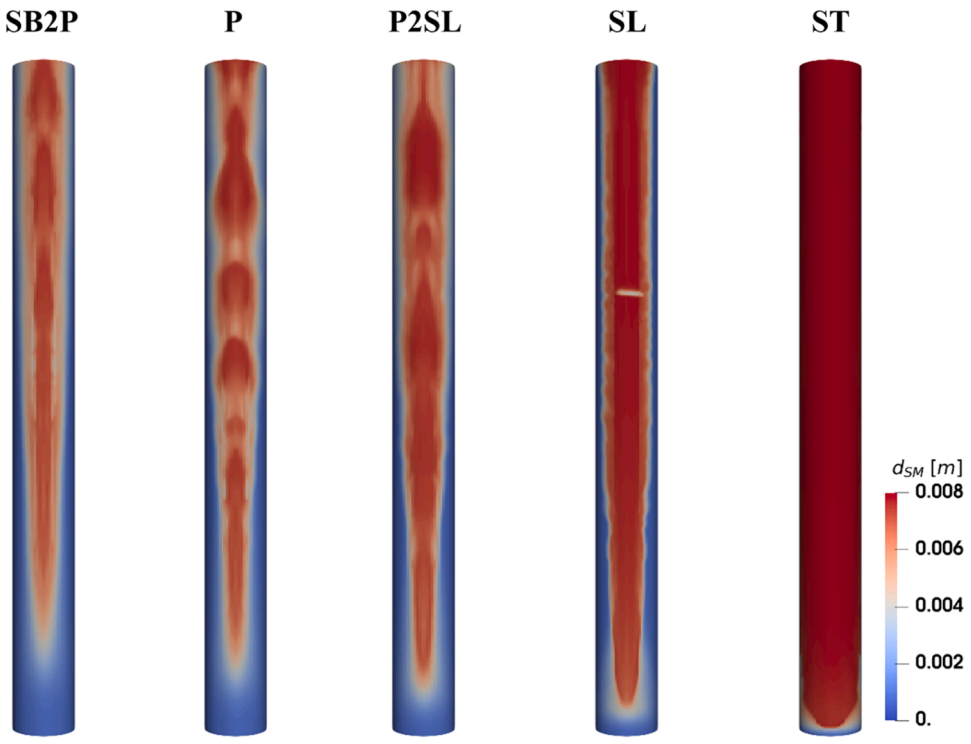

Fig. 8. View from the top of the pipe of the Sauter-mean diameter distribution in the (from left to right) stratified bubbly to plug, plug, plug to slug, slug and stratified flow regimes. Axial pipe length is scaled by a factor 0.25.

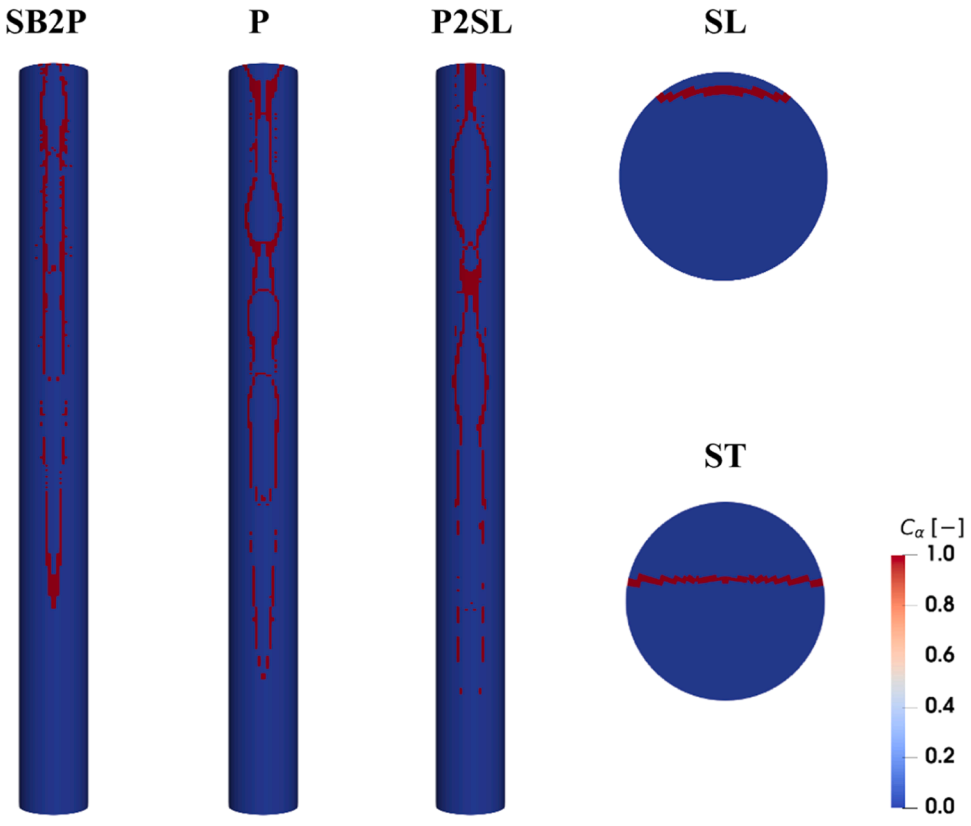

Fig. 9. View from the top of the pipe of the C_α large interface identifier in the (from left to right) stratified bubbly to plug, plug and plug to slug flow regimes, and from the front of the pipe ($L/D = 40$) in the (from top to bottom) slug and stratified flow regimes. Axial pipe length is scaled by a factor 0.25.

occupied by gas due to the higher gas fraction. After a very short distance from the inlet, completely separated gas and liquid regions are predicted (Fig. 7 – ST) and the bubble diameter quickly approaches 8 mm due to intense coalescence (Fig. 8 – ST). A large interface region separates the continuous gas and liquid regions (Fig. 9 – ST). It is interesting to note how, from the same inlet condition of uniformly distributed 1 mm bubbles, the location of the transition to large interfaces moves progressively closer to the inlet, due to increased coalescence induced by the higher void fraction moving from the SB2P to ST regimes.

Overall, the model shows a good capability to model gas bubble agglomeration in continuous clusters and predict, starting from a dispersed bubby flow at the inlet of the pipe, the development of the plug and stratified flow regimes, and the interface morphology and flow features in these regimes. More challenging is the prediction of dispersion of continuous gas into dispersed regions. This is probably the reason for the difficulty in predicting transition regimes from the bubbly to the plug flow regime (SB2P), and from the plug to the stratified through the slug regime, where an early transition to stratified flow is predicted. Also, in the plug regime, gas plugs are quite well defined, and only limited partially dispersed regions are found between them (Fig. 7 – P). Agglomeration is favoured by the interface compression, and the present results suggest a companion mechanism that instead promotes dispersion may be needed to predict mixed flow conditions with dispersed and segregated regions, and the break-up of large interfaces.

Although quantitative measurements outside of the bubbly regime are not provided in Bottin et al. (2014), the liquid velocity profiles shown in Fig. 10 for the plug and slug regimes allows at least a qualitative comparison with the literature work of Mimouni et al. (2017). A direct comparison is not possible, but the weighted-average ($\langle U_{z,w} \rangle = \langle (1-\alpha) \cdot U_{z,w} \rangle / \langle 1-\alpha \rangle$ profiles of the liquid velocity show similar behaviours with respect to the RANS results of Mimouni et al. (2017). In the plug regime, the parabolic profile is maintained, although the symmetry of the profile is broken and the velocity is much higher in the upper half of the pipe due to the presence of the intermittent gas plugs. In the slug regime, the velocity increases from the bottom to the top of the pipe and peaks at the upper wall, although GEMMA predicts a less flat profile and a steeper increase of the liquid velocity.

As mentioned, quantitative measurements outside of the bubbly regime are not available in Bottin et al. (2014). However, different models for the velocity of elongated and Taylor bubbles in the slug and plug flow regimes have been developed in the literature and allow assessment of the quantitative prediction of these parameters by a CFD model. Models are usually based on the drift flux approach:

$$U_g = C_0 \cdot j + U_{gj} \tag{18}$$

where U_g is the velocity of the gas bubble, $j = j_w + j_a$ is the volumetric flux and U_{gj} is the drift velocity. Gregory and Scott (1969) derived a simple expression with the drift velocity equal to 0:

$$U_g = 1.35 \cdot j \tag{19}$$

Wang et al. (2007), based on air-water data in a 133 m long horizontal pipe flow of 0.5 m diameter, proposed values of C_0 and U_{gj} based on the Froude number ($Fr = U_m / \sqrt{gD}$). Different values are suggested for Fr, both higher and lower than 3.5, and based on measurements at distances from the inlet of x/D 1157 and 2609. Taking values for the lower distance and $Fr < 3.5$, the model of Wang et al. (2007) reads:

$$U_g = 1.096 \cdot j + 0.342 \cdot \sqrt{g \cdot D} \tag{20}$$

Models similar to that of Wang et al. (2007) were developed by Da Silva et al. (2010), using air-water data in a 9 m long horizontal pipe of 0.026 m diameter:

$$U_g = 1.22 \cdot j + 0.34 \tag{21}$$

and Abdulkadir et al. (2020) from measurements of air-silicon oil flow in a 6 m long horizontal pipe of 0.067 m diameter:

$$U_g = 1.18 \cdot j + 0.34 \cdot \sqrt{g \cdot D} \tag{22}$$

Comparison of GEMMA results with these models for the P, P2SL and SL cases is shown in Fig. 11. The GEMMA results were obtained by

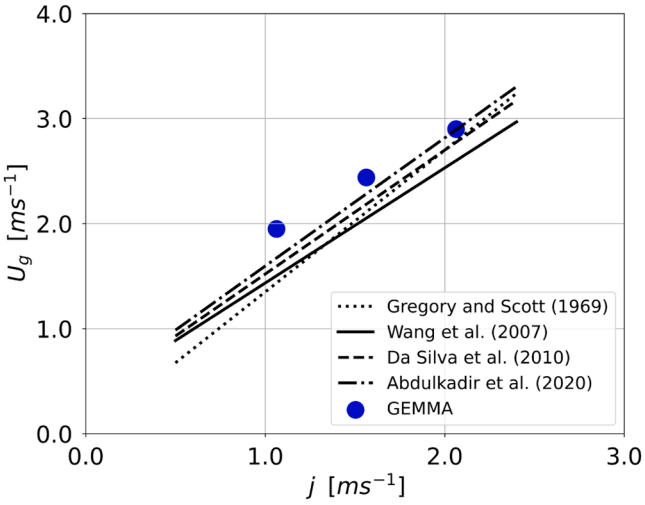

Fig. 11. Prediction of gas velocity from the GEMMA model in the P, P2SL and SL regimes compared against literature correlations for elongated and Taylor bubbles.

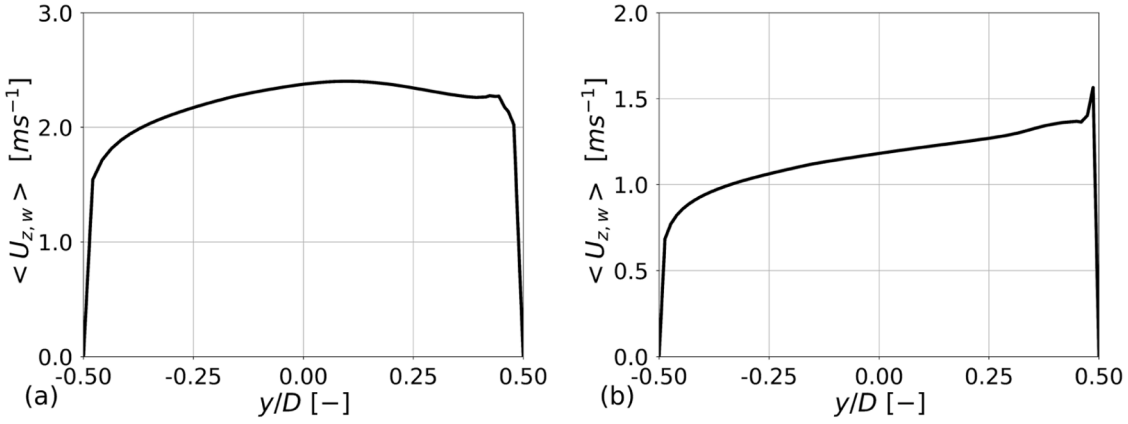

Fig. 10. Weighted average liquid velocity vertical profiles at $L/D = 40$ for the plug (P, (a)) and the slug (SL, (b)) regimes.

averaging velocity in time and over all computational cells of the domain belonging to a continuous gas region (identified by imposing $\alpha > 0.5$) and excluding the developing region at the inlet of the pipe. Good agreement is found for the velocity of plugs, where predictions are inside the range of results provided by the correlations. Discrepancies start to appear in the transition to slug regime, where the velocity is slightly higher with respect to the correlations, and becomes significant for the slug regime, where the GEMMA model overestimates the gas velocity. These results are consistent with the volume fraction distributions in Fig. 7 and confirm the capability of the model to predict the plug regime and the challenges found when predicting the slug regime, for which an earlier transition to stratified flow is obtained. It is interesting to note how the CFD results are more in agreement with models derived from data in pipes of comparable length, while the largest discrepancies are found with the correlation of Wang et al. (2007), based on experiments in a much longer pipe, where it was observed that the velocity and length of elongated bubbles were still evolving after a significant distance from the inlet. While the model is unable to predict the slug development in the METERO configuration, future investigations can target longer pipes. A longer length may enable the appearance of a delayed slug transition, which cannot be detected in the present configuration given the relatively short length of the pipe.

5.4. Mesh sensitivity in segregated regimes

The sensitivity of results to the computational mesh employed was demonstrated for the bubbly regime in Section 4, and the mesh with 560,000 elements was used for the following simulations. It is useful to extend the analysis to segregated regimes and study the impact of mesh refinement in the plug and slug regimes. Mesh convergence should indeed be expected in the dispersed bubbly regime. Instead, the resolution of large interfaces introduces further complications, as any further refinement of the grid enables the resolution of progressively smaller scales, and mesh convergence in the traditional sense may never be reached until all the scales are resolved.

The instantaneous volume fraction distribution in the plug regime (P) for the three meshes tested in Section 4 is shown in Fig. 12. As it is possible to see, the coarsest mesh does not allow the prediction of intermittent plugs even though large interfaces are detected. This is due to larger numerical diffusion and less cells containing large interfaces detected because of the mesh resolution threshold (Eq. (4)) being also active together with the condition on the bubble length scale (Eq. (5)). Instead, qualitatively similar results are obtained between Mesh 2 and Mesh 3. This enables convergence to be reached on the value of the average plug velocity, which is shown in Fig. 13 for the three meshes and compared with the same models already included in Fig. 11. Mesh refinement has a larger impact on results (results between the three meshes are much more similar in the bubbly regime) and differences in instantaneous and small scale local values are still to be expected, but the model reaches convergence and provides converged average results also in the plug regime.

In the slug regime, the anticipated transition to stratified flow is always predicted with all the meshes and was also predicted with a further increase in refinement to 2,173,500 elements. This means that limitations of the model in dispersing large interfaces are responsible for the anticipated transition rather than mesh effects. Due to the transition to stratified conditions, the effect of mesh refinement is much less than in the plug flow regime (with behaviour similar to the bubbly regime), with similar values of velocity obtained. It is difficult, however, to draw conclusions until the slug regime features are properly predicted by the model.

6. Conclusions

The morphology-adaptive GEMMA CFD model has been used to predict flow regimes developing in an air-water multiphase flow inside a horizontal pipe. Data from the METERO (Bottin et al., 2014) experiment in a 5.4 m long horizontal pipe have been used to assess the model accuracy and capability to predict the development of the bubbly, plug, slug and stratified flow regimes starting from homogeneous bubbly flow inlet conditions.

In the bubbly regime, the model predicts well some features of the

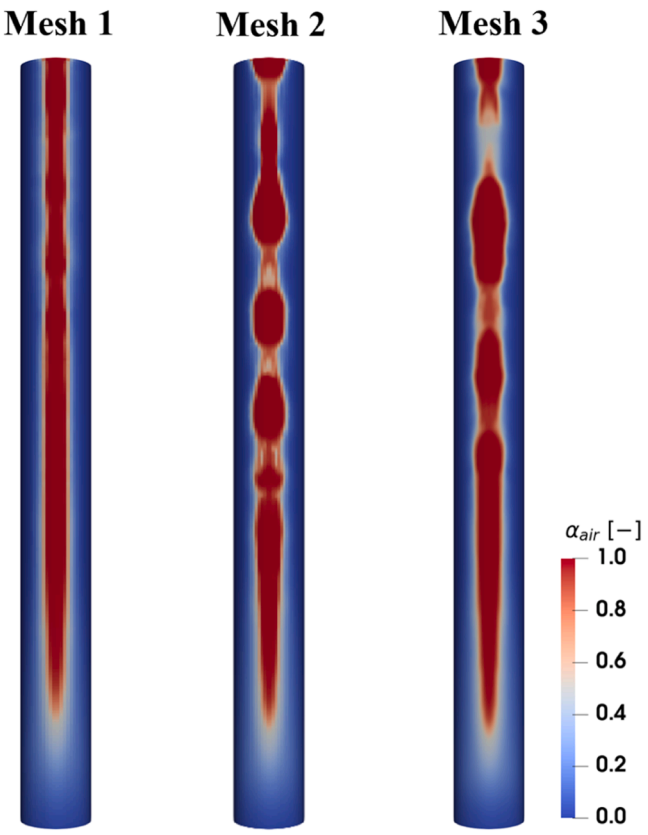

Fig. 12. View from the top of the pipe of the void fraction distribution in the plug (P) regime for (from left to right) Mesh 1, Mesh 2 and Mesh 3. Mesh 1 has 286,720 cells, Mesh 2 has 560,000 cells and Mesh 3 has 1,193,400 cells. Axial pipe length is scaled by a factor 0.25.

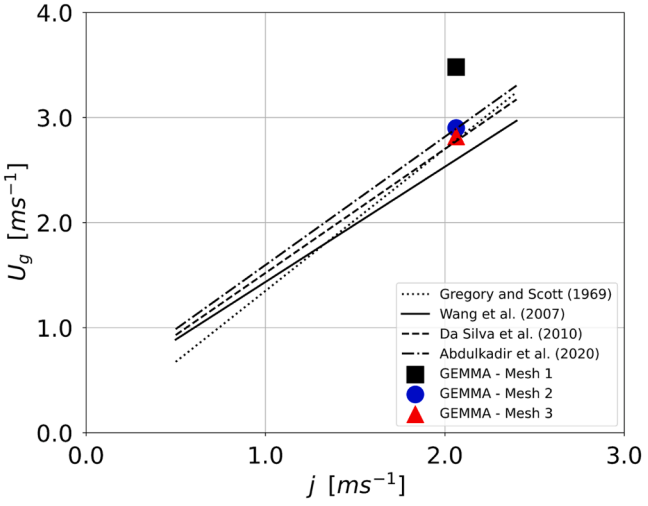

Fig. 13. Prediction of average plug velocity from the GEMMA model at different mesh refinement compared against literature correlations for elongated and Taylor bubbles. Mesh 1 has 286,720 cells, Mesh 2 has 560,000 cells and Mesh 3 has 1,193,400 cells.

flow such as the void distribution in the upper region of the pipe, and the bubble diameter. Modelling of turbulent dispersion and bubble coalescence has a strong impact on the model accuracy in these areas. In other areas, such as turbulence modelling and the flow slowing down in the upper portion of the pipe when a bubble layer is present, modelling improvements are needed. Overall, results show modelling closures that rely on relative velocity and perform well in vertical pipes where buoyancy effects are dominant may not be equipped to predict horizontal flows, where the relative velocity can be negligible, or bubbles slow down the liquid. This highlights the need for further development of the available closures.

Starting from uniformly distributed 1 mm bubbles at the inlet, the model predicts the change of the interface morphology and the development of different flow regimes depending on the phase flow rates and volume fraction. In the bubbly regime, the model operates as a standard multifluid solver, predicting the increase in void fraction at the top of the pipe. When the void fraction is increased beyond the bubbly regime, enhanced coalescence causes the bubble diameter to become larger than the threshold for segregated regimes and continuous gas regions surrounded by large scale interfaces are predicted. This enables GEMMA to successfully simulate the development of intermittent gas plugs, the increase in the length scale of the plugs approaching the transition to slug flow and the development of a stratified flow at the lowest water flow rate. The model behaves well in the bubbly, plug and stratified regimes. More challenging is the prediction of transition regions, from bubbly to plug, where a continuous film is predicted before large interfaces can be detected, and from slug to stratified, where an anticipated transition to stratified flow is predicted in the slug regime. This is attributed to excessive agglomeration and the inability of the model to properly account for dispersion and break-up of large interfaces, which may require a mechanism similar and opposite to interface compression to be predicted effectively. These findings are supported by comparison with literature models for elongated bubble velocity in horizontal pipes, showing very good accuracy in the plug regime but which deteriorates as soon as the slug region of the flow regime map is reached. When large interfaces are present, mesh effects must be carefully considered, as more local and instantaneous flow, and interface, details are resolved with any further refinement of the grid. However, GEMMA is demonstrated to provide solutions insensitive to mesh refinement for average quantities in intermittent regimes.

Overall, we believe GEMMA provides a modelling framework that can achieve accurate morphology-adaptive modelling capabilities and be applicable to the entire range of flow regimes in gas-liquid multiphase flows. In view of this, the present work provides a first demonstration of its capabilities in horizontal pipe flows. Modelling improvements in multiple areas, such as the modelling closures for bubbly flows in horizontal pipes and the dispersion of large interfaces, are necessary and have been identified. For the METERO experiment (Bottin et al., 2014), quantitative data were only available in the bubbly flow regime, and additional validation in other regimes, as well as the simulation of the entire range of horizontal regimes, will be addressed in the near future. Future studies will also need to target a wider range of flow conditions, including longer pipes and more complex geometries.

CRediT authorship contribution statement

Marco Colombo: Writing – review & editing, Writing – original draft, Validation, Software, Methodology, Funding acquisition, Conceptualization. **Michael Fairweather:** Writing – review & editing, Writing – original draft, Validation, Supervision, Methodology, Conceptualization.

Declaration of competing interest

The authors declare that they have no known competing financial interests or personal relationships that could have appeared to influence the work reported in this paper.

Acknowledgements

This work was supported by the EPSRC with the grant “Towards Comprehensive Multiphase Flow Modelling for Nuclear Reactor Thermal Hydraulics” (EP/S019871/1; EP/S019871/2). The authors also acknowledge the IT Services at the University of Sheffield and the University of Leeds for the provision of services for High Performance Computing.

Data availability

Data will be made available on request.

References

Abdulkadir, M., Zhao, D., Abdulkareem, L.A., Asikolaye, N.O., Hernandez Perez, V., 2020. Insights into the transition from plug to slug flow in a horizontal pipe: An experimental study. Chem. Eng. Res. Des. 163, 85–95.
Baker, O., 1954. Design of pipe lines for simultaneous flow of oil and gas. Oil. Gas J. 26.
Behzadi, A., Issa, R.I., Rusche, H., 2004. Modelling of dispersed bubble and droplet flow at high phase fractions. Chem. Eng. Sci. 59, 759–770.
Berberovic, E., van Hinsberg, N.P., Jakirlic, S., Roisman, I.V., Tropea, C., 2009. Drop impact onto a liquid layer of finite thickness: dynamics of the cavity evolution. Phys. Rev. E 79, 036306.
Bestion, D., 2014. The difficult challenge of a two-phase CFD modelling for all flow regimes. Nucl. Eng. Des. 279, 116–125.
Bottin, M., Berlandis, J.P., Hervieu, E., Lance, M., Marchand, M., Ozturk, O.C., Serre, G., 2014. Experimental investigation of a developing two-phase bubbly flow in horizontal pipe. Int. J. Multiphase Flow 60, 161–179.
Brackbill, J.U., Kothe, D.B., Zemach, C.C., 1992. A continuum method for modelling surface tension. J. Comput. Phys. 100, 335–354.
Burns, A.D., Frank, T., Hamill, I., Shi, J.M., 2004. 5th International Conference on Multiphase Flow, Yokohama, Japan, May 30 - June 4.
Cerne, G., Petelin, S., Tiselj, I., 2001. Coupling of the interface tracking and the two-fluid models for the simulation of incompressible two-phase flow. J. Comput. Phys. 171, 776–804.
Cheng, L., Ribatski, G., Thome, J.R., 2008. Two-phase flow patterns and flow-pattern maps: fundamentals and applications. Appl. Mech. Rev. 61, 050802.
Chinnov, E.A., Ron’shin, F.V., Kabov, O.A., 2016. Two-phase flow patterns in short horizontal rectangular microchannels. Int. J. Multiphase Flow 80, 57–68.
Cifani, P., Kuerten, J.G.M., Geurts, B.J., 2018. Highly scalable DNS solver for turbulent bubble-laden channel flow. Comput. Fluids 172, 67–83.
Collier, J.G., Thome, J.R., 1994. Convective boiling and condensation. Oxford University Press, Oxford, United Kingdom.
Colombo, M., De Santis, A., Hanson, B.C., Fairweather, M., 2022. Prediction of horizontal gas-liquid segregated flow regimes with an all flow regime multifluid model. Processes 10, 920.
Colombo, M., Fairweather, M., 2015. Multiphase turbulence in bubbly flows: RANS simulations. Int. J. Multiphase Flow 77, 222–243.
Colombo, M., Fairweather, M., 2016. RANS simulation of bubble coalescence and break-up in bubbly two-phase flows. Chem. Eng. Sci. 146, 207–225.
Colombo, M., Fairweather, M., 2019. Influence of multiphase turbulence modelling on interfacial momentum transfer in two-fluid Eulerian-Eulerian CFD models of bubbly flows. Chem. Eng. Sci. 195, 968–984.
Colombo, M., Fairweather, M., 2020. Multi-fluid computational fluid dynamic predictions of turbulent bubbly flows using an elliptic-blending Reynolds stress turbulence closure. Front. Energy Res. 8, 44.
Colombo, M., Rzehak, R., Fairweather, M., Liao, Y., Lucas, D., 2021. Benchmarking of computational fluid dynamic models for bubbly flows. Nucl. Eng. Des. 375, 111075.
Coste, P., 2013. A large interface model for two-phase CFD. Nucl. Eng. Des. 255, 38–50.
Da Silva, M.J., Hampel, U., Ramos de Arruda, L.V., Morales, R.E.M., 2010. Experimental investigation of horizontal gas-liquid slug flow by means of wire-mesh sensor. J. Braz. Soc. Mech. Sci. 33, 234–242.
De Santis, A., Colombo, M., Hanson, B.C., Fairweather, M., 2021. A generalized multiphase modelling approach for multiscale flows. J. Comput. Phys. 436, 110321.
Deendarlianto, Andrianto, M., Widyaparaga, A., Dinaryanto, O., Khasani, Indarto, 2016. CFD Studies on the gas-liquid plug two-phase flow in a horizontal pipe. J. Petrol. Sci. Eng. 147, 779–787.
du Cluzeau, A., Bois, G., Leoni, N., Toutant, A., 2022. Analysis and modeling of bubble-induced agitation from direct numerical simulation of homogeneous bubbly flows. Phys. Rev. Fluids 7, 044604.
Ekambara, K., Sanders, R.S., Nandakumar, K., Masliyah, J.H., 2012. CFD modeling of gas-liquid bubbly flow in horizontal pipes: Influence of bubble coalescence and breakup. Int. J. Chem. Eng. 2012, 620463.
Fang, J., Cambareri, J.J., Brown, C.S., Feng, J., Gouws, A., Li, M., Bolotnov, I.A., 2018. Direct numerical simulation of reactor two-phase flows enabled by high-performance computing. Nucl. Eng. Des. 330, 409–419.
Feng, J., Bolotnov, I.A., 2017. Interfacial force study on a single bubble in laminar and turbulent flows. Nucl. Eng. Des. 313, 345–360.

Feng, J., Bolotnov, I.A., 2018. Effect of the wall presence on the bubble interfacial forces in a shear flow field. Int. J. Multiphase Flow 99, 73–85.
Frederix, E.M.A., Dovizio, D., Mathur, A., Komen, E.M.J., 2021. All-regime two-phase flow modeling using a novel four-field large interface simulation approach. Int. J. Multiphase Flow 145, 103822.
Frederix, E.M.A., Mathur, A., Dovizio, D., Geurts, B.J., Komen, E.M.J., 2018. Reynolds-averaged modelling of turbulence damping near a large-scale interface in two-phase flow. Nucl. Eng. Des. 333, 122–130.
Gada, V.H., Tandon, M.P., Elias, J., Vikulov, R., Lo, S., 2017. A large scale interfacial multi-fluid model for simulating multiphase flows. Appl Math Model 44, 189–204.
Gregory, G.A., Scott, D.S., 1969. Correlation of liquid slug velocity and frequency in horizontal concurrent gas-liquid slug flow. AIChE J 15, 933–935.
Hewitt, G.F., Roberts, D.N., 1969. Studies of two-phase flow patterns by simultaneous X-ray and flash photography. Atomic Energy Research Establishment Report AERE-M 2159, HMSO.
Heyns, J.A., Oxtoby, O.F., 2014. 6th European Conference on Computational Fluid Dynamics, Barcelona, Spain, 20-25 July.
Hibal, A., Kim, S.K., Park, J.H., Jung, S.Y., 2022. Development of two-phase flow regime map for thermally stimulated flows using deep learning and image segmentation technique. Int. J. Multiphase Flow 146, 103869.
Hosokawa, S., Tomiyama, A., 2009. Multi-fluid simulation of turbulent bubbly pipe flow. Chem. Eng. Sci. 64, 5308–5318.
Hosokawa, S., Tomiyama, A., Misaki, S., Hamada, T., 2002. ASME Joint U.S.-European Fluids Engineering Division Conference (FEDSM), Montreal, Canada, 14-18 July.
Ishii, M., Hibiki, T., 2006. Thermo-fluid dynamics of two-phase flow. Springer, New York, USA.
Ishii, M., Zuber, N., 1979. Drag coefficient and relative velocity in bubbly, droplet or particulate flows. AIChE J 25, 843–855.
Jin, Y., Cavero, R.F., Weiland, C., Hoffmann, M., Schluter, M., 2023. Effects of bubble-induced turbulence on interfacial species transport: a direct numerical simulation study. Chem. Eng. Sci. 279, 118934.
Kocamustafaogullari, G., Huang, W.D., 1994. Internal structure and interfacial velocity development for bubbly two-phase flow. Nucl. Eng. Des. 151, 79–101.
Kocamustafaogullari, G., Wang, Z., 1991. An experimental study on local interfacial parameters in a horizontal bubbly two-phase flow. Int. J. Multiphase Flow 17, 553–572.
Komen, E.M.J., Mathur, A., Roelofs, F., Merzari, E., Tiselj, I., 2023. Status, perspectives, and added value of high fidelity simulations for safety and design. Nucl. Eng. Des. 401, 112082.
Kren, J., Frederix, E.M.A., Tiselj, I., Mikuz, B., 2024. Numerical study of Taylor bubble breakup in counter-current flow using large eddy simulation. Phys. Fluids 36, 023311.
Kumar, S., Ramkrishna, D., 1996. On the solution of population balance equations by discretization-I. A fixed pivot technique. Chem. Eng. Sci. 51, 1311–1332.
Lahey Jr., R.T., Baglietto, E., Bolotnov, I.A., 2021. Progress in multiphase computational fluid dynamics. Nucl. Eng. Des. 374, 111018.
Lavieville, J., Merigoux, N., Guingo, M., Baudry, C., Mimouni, S., 2017. A Generalized turbulent dispersion model for bubbly flow numerical simulation in NEPTUNE_CFD. Nucl. Eng. Des. 312, 284–293.
Lehr, F., Millies, M., Mewes, D., 2002. Bubble-size distributions and flow fields in bubble columns. AIChE J. 48, 2426–2443.
Liao, Y., Oertel, R., Kriebitzsch, S., Schlegel, F., Lucas, D., 2018. A discrete population balance equation for binary breakage. Int. J. Numer. Meth. Fl 87, 202–215.
Liao, Y., Rzehak, R., Lucas, D., Krepper, E., 2015. Baseline closure model for dispersed bubbly flow: Bubble coalescence and breakup. Chem. Eng. Sci. 122, 336–349.
Lopez de Bertodano, M., 1998. Two fluid model for two-phase turbulent jet. Nucl. Eng. Des. 179, 65–74.
Luo, H., 1993. Coalescence, breakup and liquid circulation in bubble column reactors. The Norwegian Institute of Technology, Trondheim, Norway. PhD Thesis.
Luo, H., Svendsen, H.F., 1996. Theoretical model for drop and bubble breakup in turbulent dispersions. AIChE J 42, 1225–1233.
Ma, T., Lucas, D., Jakirlic, S., Frohlich, J., 2020. Progress in the second-moment closure for bubbly flow based on direct numerical simulation data. J. Fluid Mech. 883, A9.
Marschall, H., 2011. Towards numerical simulation of multi-scale two-phase flows. Technische Universitat Munchen, Munich, Germany. PhD Thesis.
Mathur, A., Dovizio, D., Frederix, E.M.A., Komen, E.M.J., 2019. A hybrid dispersed-large interface solver for multi-scale two-phase flow modelling. Nucl. Eng. Des. 344, 69–82.
Meller, R., Schlegel, F., Lucas, D., 2020. Basic verification of a numerical framework applied to a morphology adaptive multifield two-fluid model considering bubble motions. Int. J. Numer. Meth. Fl 93, 748–773.
Mer, S., Praud, O., Neau, O., Merigoux, N., Magnaudet, J., Roig, V., 2018. The emptying of a bottle as a test case for assessing interfacial momentum exchange models for Euler–Euler simulations of multi-scale gas-liquid flows. Int. J. Multiphase Flow 106, 109–124.
Mimouni, S., Fleau, S., Vincent, S., 2017. CFD calculations of flow pattern maps and LES of multiphase flows. Nucl. Eng. Des. 321, 118–131.
Nasrfard, H., Rahimzadeh, H., Ahmadpour, A., Amani, E., 2019. Simulation of intermittent flow development in a horizontal pipe. J. Fluid. Eng. 141, 121305.
Pinilla, J.A., Guerrero, E., Pineda, H., Posada, R., Pereyra, E., Ratkovich, N., 2019. CFD modeling and validation for two-phase medium viscosity oil-air flow in horizontal pipes. Chem. Eng. Commun. 206, 654–671.
Prince, M.J., Blanch, H.W., 1990. Bubble coalescence and breakup in air-sparged bubble columns. AIChE J 36, 1485–1499.
Roth, G.A., Aydogan, F., 2014. Theory and implementation of nuclear safety system codes Part I: Conservation equations, flow regimes, numerics and significant. Prog. Nucl. Energ. 76, 160–182.
Rouhani, S.Z., Sohal, M.S., 1983. Two-phase flow patterns: a review of research results Prog. Nucl. Energ. 11, 219–259.
Rzehak, R., Krepper, E., 2013. CFD modeling of bubble-induced turbulence. Int. J. Multiphase Flow 55, 138–155.
Rzehak, R., Liao, Y., Meller, R., Schlegel, F., Lehnigk, R., Lucas, D., 2021. Radial pressure forces in Euler-Euler simulations of turbulent bubbly pipe flows. Nucl. Eng. Des. 374, 111079.
Schiller, L., Naumann, Z., 1935. A drag coefficient correlation. Z. Ver. Dtsch. Ing. 77, 318–320.
Schlegel, F., Meller, R., Krull, B., Lehnigk, R., Tekavcic, M., 2023. OpenFOAM-hybrid: a morphology adaptive multifield two-fluid model. Nucl. Sci. Eng. 197, 2620–2633.
Shin, H.C., Kim, S.M., 2022. Generalized flow regime map for two-phase mini/micro-channel flows. Int. J. Heat. Mass. Tran. 196, 123298.
Strubelj, L., Tiselj, I., 2011. Two-fluid model with interface sharpening. Int. J. Numer. Meth. Eng. 85, 575–590.
Strubelj, L., Tiselj, I., Mavko, B., 2009. Simulations of free surface flows with implementation of surface tension and interface sharpening in the two-fluid model. Int. J. Heat. Fluid. Fl 30, 741–750.
Sussman, M., Almgren, S., Bell, J.B., Colella, P., Howell, L.H., Welcome, M.L., 1999. An adaptive level set approach for incompressible two-phase flows. J. Comput. Phys. 148, 81–124.
The OpenFOAM Foundation, 2021. OpenFOAM v9 User Guide.
Tryggvason, G., Bunner, B., Esmaeeli, A., Juric, D., Al-Rawahi, N., Tauber, W., Han, J., Nas, S., Jan, Y.J., 2001. A front-tracking method for the computations of multiphase flow. J. Comput. Phys. 169, 708–759.
Ubbink, O., 1997. Numerical prediction of two fluid systems with sharp interfaces. Imperial College London, London, United Kingdom. PhD Thesis.
Wang, L.S., Krull, B., Lucas, D., Meller, R., Schlegel, F., Tekavcic, M., Xu, J.Y., 2023. Simulation of droplet entrainment in annular flow with a morphology adaptive multifield two-fluid model. Phys. Fluids 35, 103312.
Wang, X., Guo, L., Zhang, X., 2007. An experimental study of the statistical parameters of gas-liquid two-phase slug flow in horizontal pipeline. Int. J. Heat. Mass Tran. 50, 2439–2443.
Wardle, K.E., Weller, H.G., 2013. Hybrid multiphase CFD solver for coupled dispersed/segregated flows in liquid-liquid extraction. Int. J. Chem. Eng. 2013, 128936.
Wu, B., Firouzi, M., Mitchell, T., Rufford, T.E., Leonardi, C., Towler, B., 2017. A critical review of flow maps for gas-liquid flows in vertical pipes and annuli. Chem. Eng. J. 326, 350–377.
Yeoh, G.H., Cheung, S.C.P., Tu, J.Y., 2012. On the prediction of the phase distribution of bubbly flow in a horizontal pipe. Chem. Eng. Res. Des. 90, 40–51.
Yeoh, G.H., Tu, J.Y., 2010. Computational techniques for multiphase flows - Basics and applications. Butterworth-Heinemann, Elsevier, Oxford, United Kingdom.
Yin, J., Zhang, T., Krull, B., Meller, R., Schlegel, F., Lucas, D., Wang, D., Liao, Y., 2023. A CFD approach for the flow regime transition in a vane-type gas-liquid separator. Int. J. Multiphase Flow 159, 104320.
Zhang, Y., Azman, A.N., Xu, K.-W., Kang, C., Kim, H.-B., 2020. Two-phase flow regime identification based on the liquid-phase velocity information and machine learning. Exp. Fluids 61, 212.
Zimmer, M.D., Bolotnov, I.A., 2019. Slug-to-churn vertical two-phase flow regime transition study using an interface tracking approach. Int. J. Multiphase Flow 115, 196–206.